RESEARCH ARTICLE

Key Points:
- A new code is developed to simulate chorus excitation
- The code can reproduce realistic features of observed chorus
- Nonlinear dynamics of chorus is important to whistler intensity modulation

Correspondence to:
X. Tao,
xtao@ustc.edu.cn

A numerical study of chorus generation and the related variation of wave intensity using the DAWN code

X. Tao[1,2]

[1] CAS Key Laboratory of Geospace Environment, Department of Geophysics and Planetary Sciences, University of Science Technology of China, Hefei, China, [2] Mengcheng National Geophysical Observatory, School of Earth and Space Sciences, University of Science and Technology of China, Hefei, China

Abstract Chorus waves play an important role in energetic electron dynamics in the inner magnetosphere. In this work, we present a new hybrid code, DAWN, to simulate the generation of chorus waves. The DAWN code is unique in that it models cold electrons using linearized fluid equations and hot electrons using particle-in-cell techniques. The simplified fluid equations can be solved with robust and simple algorithms. We demonstrate that discrete chorus elements can be generated using the code. Waveforms of the generated element show amplitude modulation or "subpackets," and the frequency sweep rate of the generated element is found to be consistent with that of observed chorus waves. Using the DAWN code, we then investigate the variation of wave intensity ($\propto B_w^2$) with respect to linear growth rates on the equatorial plane. Previous observations showed that the change in linear growth rates of whistler waves modulated by external processes such as density modulations is usually small ($\mathcal{O}(10^{-1})$), while the variation of the wave intensity is large ($\mathcal{O}(10^1 - 10^2)$). Using a chosen set of background plasma parameters, we demonstrate that a small change ($\mathcal{O}(10^{-1})$) in linear growth rates can lead to significant variation ($\mathcal{O}(10^1)$) of wave intensity only in the transition from the broadband whistler wave generation regime to the chorus wave generation regime. Our results demonstrate the importance of including nonlinear dynamics of chorus generation in understanding the whistler wave intensity modulation process in the inner magnetosphere.

1. Introduction

Chorus waves are electromagnetic emissions frequently observed in planetary magnetospheres [e.g., *Tsurutani and Smith*, 1974; *Burtis and Helliwell*, 1975; *Hospodarsky et al.*, 2008]. These waves were originally called "dawn chorus" because they sound like birds chirping in the morning if listened through equipments that convert electromagnetic signals to sound waves. The spectrogram of chorus waves typically shows a series of discrete, narrowband rising- or falling-tone elements [*Burtis and Helliwell*, 1975; *Santolík et al.*, 2003; *Li et al.*, 2011a]. The bandwidth of each element is generally very narrow (about 100 Hz in Earth's magnetosphere). The spectrogram of chorus frequently exhibits a power minimum around half of the equatorial electron cyclotron frequency, dividing chorus waves into an upper band and a lower band [*Tsurutani and Smith*, 1974; *Burtis and Helliwell*, 1975].

Previous research indicate that chorus waves might play important roles in energetic electron dynamics in the inner magnetosphere. Chorus waves can accelerate electrons to MeV energy range, causing enhancement of relativistic electron flux in the outer radiation belt [e.g., *Horne and Thorne*, 1998; *Horne et al.*, 2005]. Recent observations [e.g., *Reeves et al.*, 2013] and simulations [e.g., *Thorne et al.*, 2013] using Van Allen Probes data provide detailed evidence of the acceleration of relativistic electrons by chorus waves. Chorus waves can also scatter hundreds of eV to a few keV electrons into the loss cone, causing precipitation of energetic electrons and forming diffuse aurora [*Thorne et al.*, 2010] and pancake distributions [*Tao et al.*, 2011]. The intensity of chorus waves can also be modulated by other physical processes like density depletions or enhancements [*Li et al.*, 2011b], correspondingly the precipitating electron flux is modulated, leading to the formation of pulsating aurora [*Nishimura et al.*, 2010].

One of the puzzling facts related to the modulation of electron precipitation flux and pulsating aurora is that the variation of linear growth rates (γ) is typically small, $\delta\gamma/\gamma \sim \mathcal{O}(10^{-1})$, while the variation of wave amplitude (B_w) is large, $\delta B_w/B_w \sim \mathcal{O}(10)$ [*Li et al.*, 2011c; *Watt et al.*, 2011]. *Watt et al.* [2011] investigated the modulation of whistler mode wave linear growth rates by ultralow frequency (ULF) waves. They found that even with the largest measured ULF wave amplitude, the change in linear growth rates is on the order

of $\mathcal{O}(10^{-1})$, the exact value of which depends on the initial anisotropy. A possible explanation is given by *Coroniti and Kennel* [1970] where they showed that if a steady state system is in the so-called small-relaxation limit, where the micropulsation period is less than the electron precipitation lifetime, a small change in linear growth rate can lead to an exponential variation in precipitation flux and wave intensity (B_w^2). However, previous work suggest that chorus waves are generated by a nonlinear wave-particle interaction process [*Helliwell*, 1967; *Trakhtengerts*, 1995; *Omura et al.*, 2008]; hence, linear growth theory alone cannot describe the intensity evolution of chorus waves. In this work, we demonstrate the importance of including nonlinear dynamics of chorus waves in theories of the modulation of electron precipitation flux and whistler wave intensity.

Because of the complicated nonlinear dynamics involved, numerical simulation is a major tool to study excitation of chorus. There are currently three major numerical models to simulate chorus generation. *Nunn* [1990] developed a Vlasov hybrid simulation (VHS) technique that can be used to simulate both rising-tone or falling-tone elements [*Nunn et al.*, 1997; *Nunn and Omura*, 2012]. Narrowband assumptions are built into the VHS model of *Nunn* [1990], and the resulting code is very efficient compared with particle-in-cell codes or traditional Vlasov codes. Because of its efficiency, realistic simulation parameters can be used in VHS simulations. The major disadvantages of the VHS code are that it does not include a natural saturation mechanism and requires a seeding wave [*Nunn and Omura*, 2012]. The other two models belong to particle-in-cell (PIC)-type simulations. *Katoh and Omura* [2007] presented the first simulation of rising-tone chorus using the electron hybrid model where cold electrons are modeled by full set of fluid equations and hot electrons are handled by PIC techniques. *Hikishima et al.* [2009] used a one-dimensional full particle-in-cell code KEMPO with an inhomogeneous background magnetic field and successfully reproduced rising-tone chorus.

The purpose of this paper is to simulate the excitation of chorus and investigate the intensity variation of whistler mode waves using a new hybrid code DAWN. The DAWN code is similar to the electron hybrid model of *Katoh and Omura* [2007], but it is unique in that linearized fluid equations are employed to describe cold electron current density. The resulting equations can be solved with simple and robust numerical algorithms. Using the code, we will investigate the variation of whistler wave amplitude with linear growth rates and demonstrate the importance of including the nonlinear dynamics of chorus excitation in consideration.

2. The DAWN Code

The major assumptions used in the DAWN code are the same as those used by the electron hybrid model of *Katoh and Omura* [2007]. The cold electrons are modeled using fluid equations and hot electrons using particle-in-cell techniques [*Birdsall and Langdon*, 2004]. The code is one-dimensional in the sense that, except for the background magnetic field ($\boldsymbol{B}_0$), the spatial variation is allowed only in the z direction in the Cartesian coordinate system. Velocities of particles, however, are fully three-dimensional. In order to take into account the bounce motion of electrons, the background magnetic field is inhomogeneous with the dominant component in the z direction. Consistent with observations [e.g., *Li et al.*, 2011a], the amplitude of the wave field B_w is assumed to be much smaller than the background field B_0 with $B_w/B_0 \sim 10^{-3}$–10^{-2}. Waves are assumed to be parallel propagating in the z direction. The perpendicular variation of the wave field due to the inhomogeneous background magnetic field is ignored in the code by assuming $k_\perp \rho \ll 1$, where ρ is the Larmor radius of electrons and $k_\perp$ the perpendicular wave number.

The major component of the background magnetic field is $B_{0z}(z) = B_{0z}(0)(1 + \xi z^2)$. The parabolic function of B_{0z} represents the magnetic field near the local minimum magnetic field strength region (e.g., the equatorial plane) in planetary magnetospheres, where chorus waves are generated. For a dipole magnetic field, $\xi = 4.5/(LR_p)^2$ with L the radial distance on the equatorial plane in unit of planet radius R_p [*Helliwell*, 1967]. This form of B_{0z} can also be used with a nondipole field to investigate the local time dependence of chorus wave properties such as frequency sweep rates as demonstrated by *Tao et al.* [2012]. The x and y components of $\boldsymbol{B}_0$ are $B_{0x} = -x(dB_{0z}/dz)/2$ and $B_{0y} = -y(dB_{0z}/dz)/2$, respectively, so that $\nabla \cdot \boldsymbol{B}_0 = 0$. Note that $B_{0x}/B_{0z} \sim B_{0y}/B_{0z} \sim \mathcal{O}(\rho/L_B)$ and $\rho/L_B \ll 1$, where $L_B \sim B_0/(dB_0/dz)$ is the scale length of the background magnetic field. The field line equations can be obtained by solving

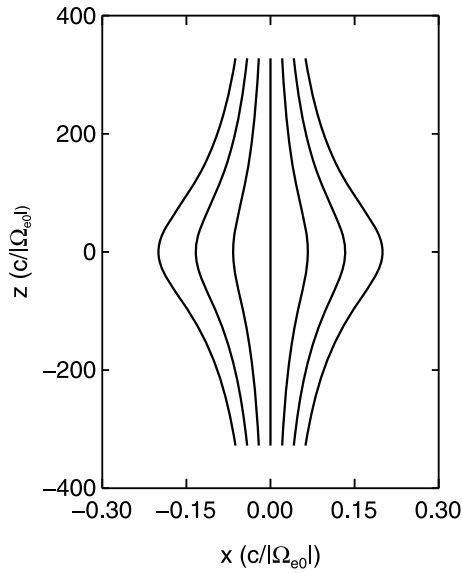$$\frac{dx}{B_x} = \frac{dy}{B_y} = \frac{dz}{B_z}, \tag{1}$$

Figure 1. Field lines of the background magnetic field at $y = 0$ of the nominal case.

which gives

$$x = \frac{x_0}{\sqrt{1 + \xi z^2}}, \tag{2}$$

$$y = \frac{y_0}{\sqrt{1 + \xi z^2}}. \tag{3}$$

where $x_0 = x(z = 0)$ and $y_0 = y(z = 0)$. The magnetic field lines of $\boldsymbol{B}_0$ with $y_0 = 0$ are given in Figure 1. To obtain B_{0x} and B_{0y} in the DAWN code, the x and y coordinates of particles are calculated from the gyroradius vector $\boldsymbol{\rho} = -\boldsymbol{u} \times \boldsymbol{e}_z / \Omega$, where $\boldsymbol{u}$ is the relativistic velocity, $\boldsymbol{e}_z$ is the unit vector in z direction, and $\Omega = qB_0/mc$ is the signed cyclotron frequency. Here c is the speed of light in vacuum, q is the charge, and m is the mass of particles. This simplified background magnetic field model has been used successfully in previous numerical studies about excitation of chorus and triggered emissions [*Nunn et al.*, 1997; *Katoh and Omura*, 2007; *Hikishima et al.*, 2009].

The electron population is assumed to consist of two components:

$$g = n_c f_c + n_h f_h, \tag{4}$$

where subscripts "c" and "h" refer to cold and hot components, respectively, and f denotes the normalized phase space density. One major difference between the DAWN code and the electron hybrid model [*Katoh and Omura*, 2007] is how the cold electron current density is calculated. *Katoh and Omura* [2007] solved the fluid momentum and continuity equations of cold electrons given by

$$\frac{\partial \boldsymbol{v}_c}{\partial t} = -(\boldsymbol{v}_c \cdot \nabla)\boldsymbol{v}_c + \frac{q}{m}\left(\boldsymbol{E} + \frac{\boldsymbol{v}_c}{c} \times \boldsymbol{B}\right), \tag{5}$$

$$\frac{\partial n_c}{\partial t} = -\nabla \cdot (n_c \boldsymbol{v}_c), \tag{6}$$

$$\boldsymbol{J}_c = q n_c \boldsymbol{v}_c, \tag{7}$$

where n is the electron density, $\boldsymbol{v}$ is the velocity, $\boldsymbol{J}$ is the current density, and $\boldsymbol{E}$ is the electric field. To simplify the numerical method of solving equations (5) and (6), we note $B_w/B_0 \ll 1$ and further assume that the nonlinear effect of cold electrons is not essential to the excitation of chorus. By linearizing equations (5)–(7), it is straightforward to show that

$$\frac{\mathrm{d}\boldsymbol{J}_c}{\mathrm{d}t} = (\omega_{pe}^2/4\pi)\boldsymbol{E} + \boldsymbol{J}_c \times \boldsymbol{\Omega}_e, \tag{8}$$

where $\boldsymbol{\Omega}_e = q\boldsymbol{B}_0/mc$ is the angular frequency vector. Equation (8) is an ordinary differential equation and can be solved using simple and robust numerical algorithms shown in Appendix A. Other equations used in the DAWN code to update wave fields are

$$\frac{\partial \boldsymbol{E}}{\partial t} = c\nabla \times \boldsymbol{B} - 4\pi\boldsymbol{J}, \tag{9}$$

$$\frac{\partial \boldsymbol{B}}{\partial t} = -c\nabla \times \boldsymbol{E}, \tag{10}$$

$$\boldsymbol{J} = \boldsymbol{J}_c + \boldsymbol{J}_h \tag{11}$$

where $\boldsymbol{J}_h$ is the hot electron current density obtained using PIC techniques [*Birdsall and Langdon*, 2004]. Since the variation of wave fields is along z direction only, $\nabla = \boldsymbol{e}_z \partial/\partial z$ in equations (9) and (10). Positions

Table 1. Simulation Parameters of the Nominal Case

Parameter	Value
Cell size	$0.05c|\Omega_{e0}|^{-1}$
Number of cells	6554
Number of masking cells at each end	300
Time step	$0.02\,|\Omega_{e0}|^{-1}$
Number of time steps	5×10^5
Number of particles per cell	2000
Cold electron plasma frequency ω_{pe}	$5\,|\Omega_{e0}|$
Density ratio n_h/n_c	6×10^{-3}
Parallel thermal velocity $w_\parallel$	$0.2c$
Perpendicular thermal velocity $w_\perp$	$0.53c$
The inhomogeneity parameter ξ	$8.62 \times 10^{-5}\,c^{-2}\Omega_{e0}^2$

and velocities of hot electrons are simply updated by solving the relativistic Lorentz equations using Boris method [*Birdsall and Langdon*, 2004, pp. 356–357]. Since we are investigating chorus waves with frequency much larger than the ion cyclotron frequency, ions are treated as fixed. The detailed numerical algorithm of solving field equations is shown in Appendix A, and validation of the numerical code is presented in Appendix B.

The hot electron distribution used by *Katoh and Omura* [2007] and *Hikishima et al.* [2009] is a loss cone distribution with temperature anisotropy. The use of a loss cone distribution can be helpful to study the precipitation of electrons in generation of chorus [e.g., *Hikishima et al.*, 2010]. On the other hand, the loss cone is not essential to the generation of whistler mode waves, which is the focus of this work; hence, we choose the hot electron distribution to be bi-Maxwellian on the equatorial plane for simplicity:

$$f_h(u_\parallel, u_\perp) = \frac{1}{(2\pi)^{3/2} w_\parallel w_\perp^2} \exp\left(-\frac{u_\parallel^2}{2w_\parallel^2} - \frac{u_\perp^2}{2w_\perp^2} \right), \tag{12}$$

where $w_\parallel$ and $w_\perp$ are the parallel and perpendicular thermal velocities in the nonrelativistic limit. By using a bi-Maxwellian distribution, the numerical code is simplified because we can avoid removing particles from the simulation system as needed by *Hikishima et al.* [2009]. The distribution of hot electrons at other latitudes is obtained by the conservation of the first adiabatic invariant and energy, as shown in Appendix C.

Absorbing boundary conditions are implemented for waves. A masking function is used to damp wave fields near the simulation boundary. In this work, we multiply the current density and the electric fields by

$$g(x) = \begin{cases} \sin(\pi x/2L_d), & \text{if } x \le L_d, \\ 1, & \text{otherwise,} \end{cases} \tag{13}$$

where x is the distance to the two boundaries and L_d is the length of the damping region at each end of the simulation domain. For particle boundary conditions, we follow *Hikishima et al.* [2009] and simply reflect charged particles as they cross the boundary. This is roughly consistent with the bounce motion of charged particles in the background magnetic field.
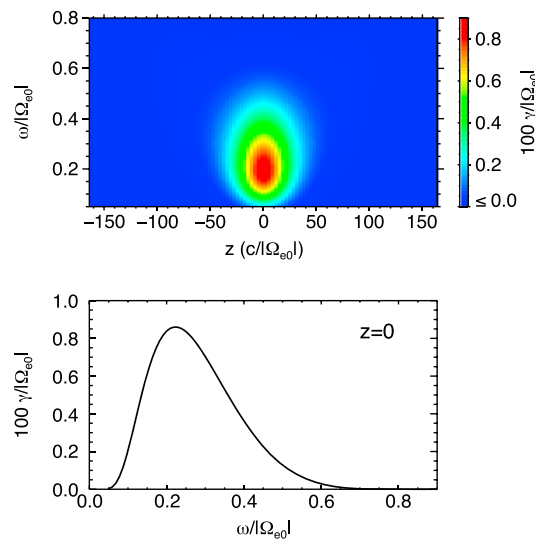
3. Simulation Results

Simulations results, normalized by c, $|\Omega_{e0}| \equiv |\Omega_e(z = 0)|$, and $B_{0z}(z = 0)$, are presented in this section. We first present a "nominal" case study showing the generation of chorus waves and its characteristics using the DAWN code in section 3.1. Then we investigate the variation of wave intensity with respect to the linear growth rate by performing five simulations with different choices of initial temperature anisotropy in section 3.2. The computation time of each simulation in the present study is about 2 days with 12 processors (3.06 GHz).

3.1. A Case Study

A relatively large value of the inhomogeneity factor ξ is used in this paper so that the wave field can saturate within the simulation domain. We choose

Figure 2. (top) Two-dimensional linear growth rates as a function of distance z and wave frequency ω of the nominal case. (bottom) Linear growth rate γ at $z = 0$ as a function of wave frequency ω.
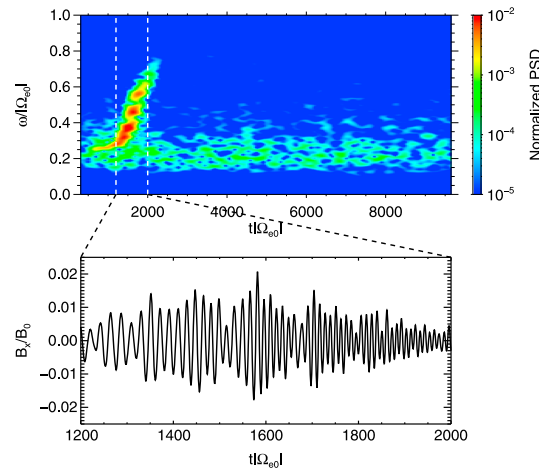
Figure 3. (top) The chorus wave element observed at $z \approx -25c|\Omega_{e0}|^{-1}$ of the nominal case. (bottom) The x component of the wave magnetic field from $t|\Omega_{e0}| = 1200$ to $t|\Omega_{e0}| = 2000$ showing modulation of wave amplitude.

$\xi = 8.62 \times 10^{-5}c^{-2}\Omega_{e0}^2$, which corresponds to $R_p = R_E/32$ with $L = 4$ in a dipole field. Because ξ used is 1024 times larger than ξ of the terrestrial dipole field, a higher temperature anisotropy than those typically observed in space plasmas is needed to excite chorus waves. This is consistent with results of *Katoh and Omura* [2013], since a larger inhomogeneity factor means a larger wave amplitude threshold for the excitation of chorus. We have also performed simulations with a ξ that is 4 times smaller than the one used in this paper, and the minimum temperature anisotropy needed to excite chorus is about 1.2 (not shown). Other parameters of the simulation are shown in Table 1.

The two-dimensional linear growth rates as a function of z and ω are calculated using *Xiao et al.* [1998] for the nominal case and are shown in Figure 2 (top). The linear growth rates on the equatorial plane ($z = 0$) are shown in Figure 2 (bottom). The linear growth rates quickly decrease with increasing $|z|$, because of the reduced temperature anisotropy and hot electron number density as shown in Appendix C. Note that γ reduces to about 0 at $|z| \approx 60c|\Omega_{e0}|^{-1}$, where the convective growth of whistler mode waves stops and the time-averaged wave intensity reaches a maximum value (not shown).

Using wave fields recorded at $z = -25c|\Omega_{e0}|^{-1}$, we plot the frequency-time spectrogram showing the generated chorus element in Figure 3. In Figure 3 (top), a strong rising-tone discrete element is seen together with a much weaker background whistler waves. Note that in terrestrial magnetosphere, chorus waves normally consist of a series of discrete elements, while there is only one such element in Figure 3. One possible reason might be that, with current simulation parameters, there is not enough free energy of hot electrons to generate a second element. Indeed, a simulation with $u_\perp = 0.57c$ and hence a larger temperature anisotropy generated multiple elements (not shown). Further development of chorus wave theory is required to explain what determines the number of elements in chorus waves.

The element in Figure 3 has a nearly constant-tone part from about $t|\Omega_{e0}| = 500$ to 1200, followed by an upward chirping discrete element. Note that the central frequency of the leading constant tone and, correspondingly, the starting frequency of the upward chirping element is about $0.26 |\Omega_{e0}|$. *Hikishima et al.* [2009] concluded that the starting frequency of rising-tone elements corresponds to the lowest unstable frequency determined by the linear growth theory. In this case, however, the starting frequency is closer to the wave frequency with maximum linear growth rate on the equatorial plane (Figure 2, bottom), which is about $\omega(\gamma_{max}) \approx 0.22 |\Omega_{e0}|$, than the lowest unstable frequency. The factors that determine the starting frequency of the discrete element will be explored in a separate publication.

To estimate whether the numerically generated chorus element has a reasonable frequency sweep rate ($\Gamma \equiv d\omega/dt$), we now calculate Γ of the element and compare that with a previous theory by *Helliwell* [1967]. *Tao et al.* [2012] compared the theory of *Helliwell* [1967] with satellite observations and demonstrated that the frequency sweep rate of *Helliwell* [1967] is about a factor of 2 smaller than that from observations. For $\omega = 0.3|\Omega_{e0}|$, *Tao et al.* [2012] showed that

$$\Gamma_H/2\pi \approx 0.48 f_{ce0}^{2/3} \xi^{2/3} v_{res}^{4/3}, \qquad (14)$$

where $f_{ce0} \equiv |\Omega_{e0}|/2\pi$ and v_{res} is the resonant velocity corresponding to $\omega = 0.3|\Omega_{e0}|$. From Figure 3 (top), the frequency sweep rate of the element can be estimated by noting that the central frequency of the element (ω_c) is about $0.27 |\Omega_{e0}|$ at $t|\Omega_{e0}| = 1200$, and

Table 2. Anisotropy and Maximum Linear Growth Rates of All Cases

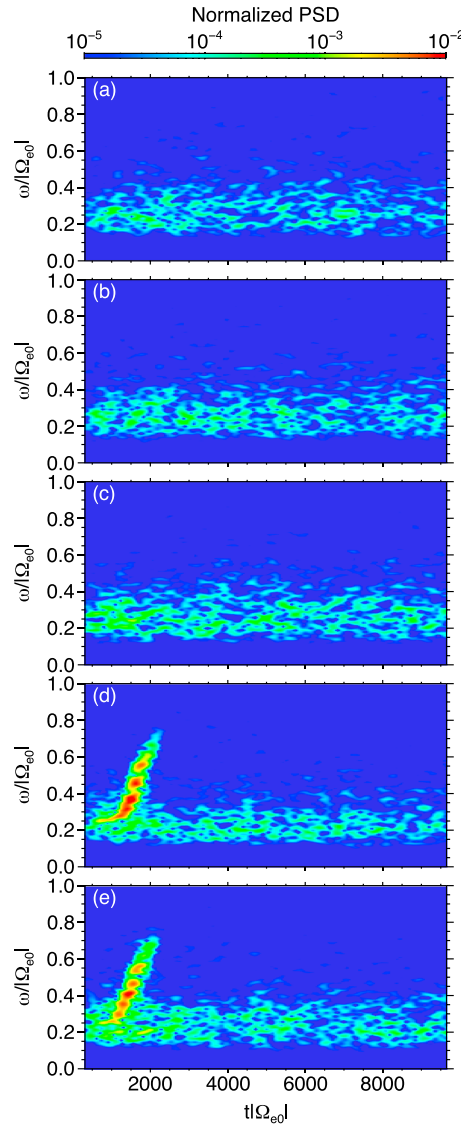| Case	(a)	(b)	(c)	(d)	(e)
$w_\perp/c$	0.47	0.49	0.51	0.53	0.55
Anisotropy	4.52	5.00	5.50	6.02	6.56
$100\gamma_{max}/|\Omega_{e0}|$	0.52	0.62	0.73	0.86	1.00

Figure 4. The power spectrogram of wave magnetic field recorded at $z \approx -25c|\Omega_{e0}|^{-1}$ from five different runs with parameters given in Tables 1 and 2. Color coded is the normalized wave power spectral density.
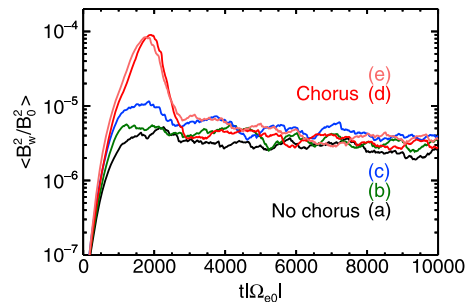

Figure 5. The time evolution of spatially averaged normalized wave magnetic field intensity of five cases.

$\omega_c \approx 0.63|\Omega_{e0}|$ at $t|\Omega_{e0}| = 2000$. Correspondingly, $\Gamma = \Delta\omega_c/\Delta t \approx 4.5 \times 10^{-4} \Omega_{e0}^{-2}$. From equation (14), $\Gamma_H \approx 2.2 \times 10^{-4} \Omega_{e0}^{-2}$; hence, $\Gamma/\Gamma_H \approx 2.05$. This conclusion is consistent with that of *Tao et al.* [2012], indicating that the frequency sweep rate of discrete element generated by the DAWN code is consistent with observations.

The waveform of the element from $t|\Omega_{e0}| = 1200$ to 2000 is shown in Figure 3 (bottom). It clearly demonstrates the amplitude modulation of the element, forming the so-called chorus subpackets, which have been observed by satellite [e.g., *Santolík et al.*, 2004]. Figure 3 further demonstrates that the DAWN code is capable of reproducing realistic features of observed chorus elements.

3.2. The Amplitude Variation
In this section, we will investigate the variation of whistler wave intensity with respect to the linear growth rate. We perform five simulations in total with different initial perpendicular thermal velocities and hence different temperature anisotropies. Other simulation parameters are the same as the nominal case. The profiles of the linear growth rate look similar to the one shown in Figure 2, with different maximum unstable frequencies and maximum linear growth rates. The maximum linear growth rates of all five cases are listed in Table 2. The frequency-time spectrograms of the generated wave fields plotted using data at $z = -25c|\Omega_{e0}|^{-1}$ of all five cases are shown in Figure 4. To simplify discussions, we define two generation regimes according to the type of wave fields generated: one is the broadband whistler wave regime (cases (a)–(c)) and the other is chorus wave regime (cases (d) and (e)). In broadband whistler wave regime, whistler waves with no discrete structures, typically driven by temperature anisotropy, are generated; in chorus wave regime, discrete elements with frequency chirping are present. Among these five simulations, case (d) is the one studied in detail in section 3.1.

We use the average magnetic field energy density K^B to characterize wave intensity, and

$$K^B = \sum_i \frac{B_{ix}^2 + B_{iy}^2}{N_g B_0^2}, \quad (15)$$

where the summation is performed along all grid points whose total number is N_g. Figure 5 presents the evolution profile of K^B with time for all five cases. Cases (a)–(c) show the usual wave intensity evolution [e.g., *Ossakow et al.*, 1972] with a linear growth phase followed by saturation of the wave field starting from about $t|\Omega_{e0}| = 1000$. Cases (d) and (e), however, show different evolution profiles of K^B in that there is a dramatic increase in K^B starting from $t|\Omega_{e0}| \approx 1000$,
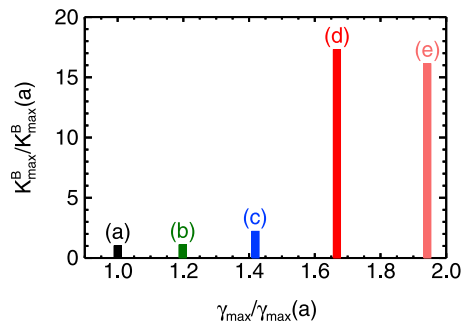
Figure 6. The maximum average wave magnetic field intensity as a function of maximum linear growth rates. Variables from case (a) are used as the normalization units.

corresponding to the excitation of chorus elements as can be seen from Figure 4. The wave intensity K^B reaches a peak near $t|\Omega_{e0}| \approx 1800$ and then quickly reduces to a level comparable to those of cases (a)–(c) at $t|\Omega_{e0}| \approx 3000$. Figure 5 indicates that, compared with broadband whistler waves of cases (a)–(c), chorus might be viewed as a much more violent way of releasing free energy of the plasma.

To show the variation of wave intensity with linear growth rates, we plot in Figure 6 the maximum average magnetic field energy density K^B_{max}, normalized by K^B_{max} of case (a), as a function of the maximum linear growth rate γ_{max}, normalized by γ_{max} of case (a). From case (a) to case (b), an increase in γ_{max} by about 0.2 leads to an increase in K^B_{max} by about 0.08. From case (a) to case (c), $\delta\gamma_{max}/\gamma_{max}(a) \approx 0.40$, and $\delta K^B_{max}/K^B_{max}(a) \approx 1.2$. The most significant increase in K^B_{max} from case (a) occurs in case (d), where a chorus element is generated. From case (a) to case (d), $\delta\gamma_{max}/\gamma_{max}(a) \approx 0.66$, and $\delta K^B_{max}/K^B_{max}(a) \approx 16$. We note that a further increase of γ_{max} from case (d) to case (e) does not lead a dramatic change in K^B_{max}. An increase in the initial temperature anisotropy leads to a slight decrease of K^B_{max} from case (d) to case (e), which indicates that in the chorus wave generation regime, the wave intensity might not be solely determined by temperature anisotropy. How the temperature anisotropy affects the maximum amplitude of chorus waves and the variation of wave intensity in the chorus wave generation regime will be investigated in a future work.

Figure 6 clearly demonstrates the importance of including nonlinear growth of chorus waves in theories of whistler wave intensity modulation and the related electron precipitation flux modulation [e.g., *Coroniti and Kennel*, 1970]. *Watt et al.* [2011] showed that the modulation by ULF waves can only cause a small change in linear growth rates, $\delta\gamma/\gamma \sim \mathcal{O}(10^{-1})$. A similar amount of change in γ has also been shown by *Li et al.* [2011c, 2011b]. On the other hand, the wave amplitude variation, as demonstrated by *Li et al.* [2011c, 2011b], is $\delta B_w/B_w \sim \mathcal{O}(10)$. Figure 6 demonstrates that the amount of change in B_w or K^B, for a given amount of $\delta\gamma$, depends on the state of the system. In the broadband whistler wave generation regime (cases (a)–(c)) or chorus wave regime (cases (d) and (e)), a small change in γ only causes a small variation in wave intensity. The largest variation of wave intensity for a given amount of variation in γ occurs in the transition from the broadband whistler wave regime to the chorus wave regime.

4. Summary

We presented a new hybrid code, DAWN, to simulate excitation of chorus waves. The DAWN code uses linearized fluid equations for cold electrons and the PIC technique for hot electrons. The linearized fluid equations can be solved using simple and robust numerical algorithms. This way of handling cold electrons should be applicable to other problems where nonlinearity of the fluid component is not essential. Compared with the full particle code of *Hikishima et al.* [2009], the hybrid approach of the DAWN code allows the use of fewer particles, and hence shorter simulation time. Compared with the electron hybrid model of *Katoh and Omura* [2007], the DAWN code solved linearized fluid equations to calculate cold electron current density and used reflecting boundary conditions for particles. In the electron hybrid model, full fluid equations of cold electrons are used, and fresh electrons are supplied from the boundaries into the simulation domain to maintain the initial velocity distribution.

The generated wave element using the DAWN code demonstrates realistic features of observed chorus in that the discrete element is narrowband and quasi-coherent with amplitude modulation. The frequency sweep rate (Γ) of the generated chorus element is about 2 times larger than the theoretical frequency sweep rate (Γ_H) of *Helliwell* [1967]. Because *Tao et al.* [2012] demonstrated that Γ_H is about 2 times smaller than the frequency sweep rate of observed chorus elements, the generated element from the DAWN code has a frequency sweep rate consistent with observations. We conclude that the DAWN code is able to reproduce realistic features of chorus waves and should find broad applications in the study of chorus excitation.

We then used the DAWN code to investigate the variation of wave intensity before and after chorus excitation with the linear growth rate. We demonstrated that in the broadband whistler wave regime and the chorus regime, a small change in linear growth rates, $\delta\gamma/\gamma \sim \mathcal{O}(10^{-1})$, leads to similar amount of change in wave amplitude; i.e., $\delta B_w/B_w \sim \mathcal{O}(10^{-1})$. The most dramatic change of wave intensity occurs in the transition from the broadband whistler wave regime to the chorus regime. The resulting chorus elements typically have a maximum wave intensity that is an order of magnitude larger than those in the broadband whistler wave regime, despite $\delta\gamma/\gamma \sim \mathcal{O}(10^{-1})$. This indicates that it is important to include the nonlinear growth of chorus waves in theoretical models of wave intensity modulation and the related electron precipitation flux modulation.

Appendix A: The Numerical Algorithm of Solving Field Equations

In the one-dimensional DAWN code, the Maxwell equations (9) and (10) are solved by the finite difference time domain algorithm [*Inan and Marshall*, 2011], where we place components of $\boldsymbol{E}$ field at spatial grid j and time step n, and components of $\boldsymbol{B}$ field at spatial grid $(j + 1/2)$ and time step $(n + 1/2)$. We use the standard notation here that spatial grid j refers to $z = j\Delta z$ and time step n refers to $t = n\Delta t$, with Δz the spatial grid size and Δt the time step. The current components J_x and J_y are colocated with $\boldsymbol{E}$ components but are updated at time step $(n + 1/2)$. To update $\boldsymbol{E}$ and $\boldsymbol{B}$ fields, we discretize the Maxwell equation as

$$\left.\frac{\partial E_x}{\partial t}\right|_j^{n+\frac{1}{2}} = -c\left.\frac{\partial B_y}{\partial z}\right|_j^{n+\frac{1}{2}} - 4\pi J_x\Big|_j^{n+\frac{1}{2}}, \tag{A1}$$

$$\left.\frac{\partial E_y}{\partial t}\right|_j^{n+\frac{1}{2}} = c\left.\frac{\partial B_x}{\partial z}\right|_j^{n+\frac{1}{2}} - 4\pi J_y\Big|_j^{n+\frac{1}{2}}, \tag{A2}$$

$$\left.\frac{\partial B_x}{\partial t}\right|_{j+\frac{1}{2}}^{n} = c\left.\frac{\partial E_y}{\partial z}\right|_{j+\frac{1}{2}}^{n}, \tag{A3}$$

$$\left.\frac{\partial B_y}{\partial t}\right|_{j+\frac{1}{2}}^{n} = -c\left.\frac{\partial E_x}{\partial z}\right|_{j+\frac{1}{2}}^{n}, \tag{A4}$$

where

$$\left.\frac{\partial E}{\partial t}\right|_j^{n+\frac{1}{2}} = \frac{E_j^{n+1} - E_j^n}{\Delta t}, \tag{A5}$$

$$\left.\frac{\partial E}{\partial z}\right|_{j+\frac{1}{2}}^{n} = \frac{E_{j+1}^n - E_j^n}{\Delta z}, \tag{A6}$$

$$\left.\frac{\partial B}{\partial t}\right|_{j+\frac{1}{2}}^{n} = \frac{B_{j+\frac{1}{2}}^{n+\frac{1}{2}} - B_{j+\frac{1}{2}}^{n-\frac{1}{2}}}{\Delta t}, \tag{A7}$$

$$\left.\frac{\partial B}{\partial z}\right|_j^{n+\frac{1}{2}} = \frac{B_{j+\frac{1}{2}}^{n+\frac{1}{2}} - B_{j-\frac{1}{2}}^{n+\frac{1}{2}}}{\Delta z}. \tag{A8}$$

Here E and B denote either x or y component of the electric and magnetic field, respectively. Note that to avoid self-force [*Birdsall and Langdon*, 2004], we need to use $\boldsymbol{B}$ at spatial grid j, obtained from spatial grids $(j \pm 1/2)$ by $B_j = (B_{j+1/2} + B_{j-1/2})/2$, in Lorentz equations.

To update the cold electron current density equation (8), we use

$$\left.\frac{dJ_x}{dt}\right|^{n} = (\omega_{pe}^2/4\pi)E_x^n + J_y^n\Omega_e, \tag{A9}$$

$$\left.\frac{dJ_y}{dt}\right|^{n} = (\omega_{pe}^2/4\pi)E_y^n - J_x^n\Omega_e, \tag{A10}$$

where

$$\left.\frac{dJ}{dt}\right|^n = \frac{J^{n+\frac{1}{2}} - J^{n-\frac{1}{2}}}{\Delta t}, \tag{A11}$$

$$J^n = \frac{J^{n+\frac{1}{2}} + J^{n-\frac{1}{2}}}{2}. \tag{A12}$$

Here J can be either J_x or J_y. Equations (A9)–(A12) can be solved together to give

$$J_x^{n+\frac{1}{2}} = A_x/a, \tag{A13}$$

$$J_y^{n+\frac{1}{2}} = A_y/a, \tag{A14}$$

where

$$A_x = -J_x^{n-\frac{1}{2}}\left(\frac{\Omega_e \Delta t}{2} - \frac{2}{\Omega_e \Delta t}\right) + 2J_y^{n-\frac{1}{2}}$$
$$+ \frac{\omega_{pe}^2}{4\pi}\left(\frac{2}{\Omega_e}E_x^n + \Delta t E_y^n\right) \tag{A15}$$

$$A_y = -J_y^{n-\frac{1}{2}}\left(\frac{\Omega_e \Delta t}{2} - \frac{2}{\Omega_e \Delta t}\right) - 2J_x^{n-\frac{1}{2}}$$
$$+ \frac{\omega_{pe}^2}{4\pi}\left(\frac{2}{\Omega_e}E_y^n - \Delta t E_x^n\right) \tag{A16}$$

$$a = \frac{\Omega_e \Delta t}{2} + \frac{2}{\Omega_e \Delta t}. \tag{A17}$$

Equation (8) has been widely used in numerical modeling of propagation of electromagnetic waves in plasmas [see, e.g., *Inan and Marshall*, 2011, p. 275]. A numerical algorithm for solving equation (8) together with Maxwell equations (9) and (10) in three dimensions is given by *Lee and Kalluri* [1999].

Appendix B: Validation of the DAWN Code

The DAWN code mainly consists of two parts: the particle mover that solves Lorentz equations to calculate particles' trajectories and the field equation solver that updates Maxwell equations to obtain electromagnetic fields from charged particle current distributions. In this section, we present the basic validation of these two parts.

B1. The Trajectory and Energy Conservation of a Bouncing Particle

One way of validating the particle mover of the DAWN code is to show that the calculated trajectory of an electron moving in an inhomogeneous background magnetic field is consistent with theory. In this calculation, we explicitly set wave fields to zero; hence, the energy of the particle should be conserved. In a parabolic field given by $B = B_0(1 + \xi z^2)$, the z component of the guiding center equations of motion is

$$m\Upsilon\frac{d^2z}{dt^2} = -\frac{\mu}{\Upsilon}\frac{\partial B}{\partial z}, \tag{B1}$$

where $\Upsilon = \sqrt{1 + (u_\parallel^2 + u_\perp^2)/c^2}$ is the relativistic factor and $\mu \equiv mu_\perp^2/2B$ is the first adiabatic invariant. Equation (B1) is an equation of a harmonic oscillator, and its solution is $z = z_0\cos(\omega_b t + \phi_0)$, where z_0 is the initial position, ϕ_0 is the initial phase angle determined by the initial position and velocity, and the bounce frequency $\omega_b = v_{\perp 0}\sqrt{\xi}$. Here $v_{\perp 0}$ is the perpendicular velocity at $z = 0$.

We choose $\xi = 0.862c^{-2}\Omega_{e0}^2$ and trace the trajectory of an electron with randomly chosen $v_\perp(t = 0) = 0.117c$, $v_\parallel(t = 0) = 0.0795c$, and $z(t = 0) = -2.62c|\Omega_{e0}|^{-1}$ for one bounce period. In Figure B1, we demonstrate that there is good agreement about the particle trajectory between simulation and theory. Also, the energy of the particle, represented by the relativistic Υ factor, is well conserved. We have verified that $(\Upsilon_{max} - \Upsilon_{min})/\Upsilon_{min} \sim 10^{-16}$, zero within machine precision.
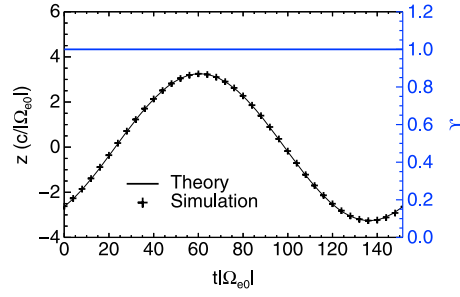
Figure B1. The validation of the Lorentz equation solver of the DAWN code. The black line and crosses demonstrate the agreement of the trajectory of a bouncing electron between theory and simulation. The blue line shows the conservation of energy when there is only background magnetic field.

B2. Cold Plasma Wave Dispersion Relation

We now validate the field equation solver of the DAWN code by showing the plasma dispersion relation of thermal noise in a homogeneous background field ($\xi = 0$) with $\omega_{pe} > |\Omega_e|$. Because of $\boldsymbol{k} \| \boldsymbol{B}_0$ and that ions are fixed, there are two R modes and one L mode. Three characteristic frequencies include one resonance frequency at $\omega = |\Omega_e|$, and two cutoff frequencies ω_R and ω_L given by

$$\omega_{\substack{R \\ L}} = \frac{|\Omega_e|}{2} \left(\pm 1 + \sqrt{1 + 4\omega_{pe}^2/\Omega_e^2} \right). \qquad (B2)$$

We choose $\omega_{pe} = 2|\Omega_e|$, $n_h/n_c = 2 \times 10^{-3}$, $w_\| = w_\perp = 0.1c$. Hot particles with a very small number density are used to generate thermal noise, because the cold electrons are modeled by fluid equations.

The agreement between the ω-k dispersion relation from the DAWN code and cold plasma wave theory [e.g., *Nicholson*, 1992, p. 159] is shown in Figure C1, which indicates the validity of the field equation solver of the DAWN code.

Appendix C: The Field Line Dependence of the Distribution of Hot Electrons

The distribution function of hot electrons in the DAWN code is given only on the equatorial plane ($z = 0$). The distribution at other positions is obtained by assuming the conservation of the first adiabatic invariant μ and the total momentum p. According to the Liouville's theorem, the distribution function g is constant for a given μ and p. To obtain $g(u_\|, u_\perp)$ at an arbitrary position, we note that the velocities at different positions for a given μ and p are related by

$$u_{\perp e}^2 = (B_e/B)u_\perp^2, \qquad (C1)$$

$$u_{\|e}^2 = u_\| + \zeta_B u_\perp^2, \qquad (C2)$$

where the subscript "e" is used in this section to denote quantities on the equatorial plane, and $\zeta_B = 1 - B_e/B$. If $g_e = n_e f_e$ with f_e given by equation (12), the distribution function $g(u_\|, u_\perp)$ is, using equations (C1) and (C2),

$$g(u_\|, u_\perp) = \frac{n_e}{(2\pi)^{3/2} w_{\|e} w_{\perp e}^2} \exp\left(-\frac{u_\|^2 + \zeta_B u_\perp^2}{2w_{\|e}^2} \right) \exp\left[-\frac{(1 - \zeta_B)u_\perp^2}{2w_{\perp e}^2} \right], \qquad (C3)$$

which can be reorganized as

$$g(u_\|, u_\perp) = \frac{n_e \zeta^2}{(2\pi)^{3/2} w_{\|e} (\zeta w_{\perp e})^2} \cdot \exp\left(-\frac{u_\|^2}{2w_{\|e}^2} \right) \exp\left[-\frac{u_\perp^2}{2(\zeta w_{\perp e})^2} \right], \qquad (C4)$$

where

$$\zeta^2 = \left[1 + \left(w_{\perp e}^2/w_{\|e}^2 - 1 \right) \zeta_B \right]^{-1}. \qquad (C5)$$

Equation (C4) corresponds to a bi-Maxwellian distribution

$$g(u_\|, u_\perp) = \frac{n}{(2\pi)^{3/2} w_\| w_\perp^2} \cdot \exp\left(-\frac{u_\|^2}{2w_\|^2} \right) \exp\left(-\frac{u_\perp^2}{2w_\perp^2} \right), \qquad (C6)$$
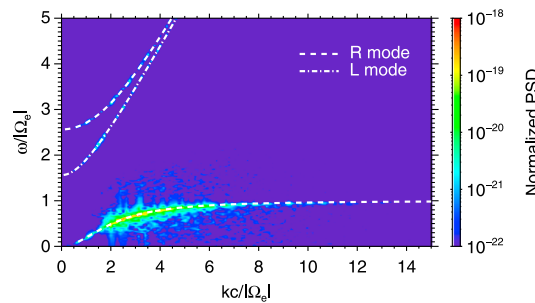

Figure C1. The comparison of the ω-k dispersion relation in a homogeneous plasma between the DAWN code simulation results and the cold plasma wave theory denoted by white lines. Color coded is the normalized power spectral density of the magnetic field fluctuations from simulation. Dash lines denote R-mode waves, and the dash-dotted line denotes the L-mode wave.

with $n = \zeta^2 n_e$, $w_\parallel = w_{\parallel e}$, and $w_\perp = \zeta w_{\perp e}$. For the field line dependence of other types of distribution functions, we refer readers to *Xiao and Feng* [2006].

References

Birdsall, C. K., and A. B. Langdon (2004), *Plasma Physics via Computer Simulation,* 1st ed., Series in Plasma Physics, Taylor and Francis, London, U. K.

Burtis, W. J., and R. A. Helliwell (1975), Magnetospheric chorus: Amplitude and growth rate, *J. Geophys. Res.*, *80*(22), 3265–3270, doi:10.1029/JA080i022p03265.

Coroniti, F. V., and C. F. Kennel (1970), Electron precipitation pulsations, *J. Geophys. Res.*, *75*(7), 1279–1289, doi:10.1029/JA075i007p01279.

Helliwell, R. A. (1967), A theory of discrete VLF emissions from the magnetosphere, *J. Geophys. Res.*, *72*(19), 4773–4790.

Hikishima, M., S. Yagitani, Y. Omura, and I. Nagano (2009), Full particle simulation of whistler-mode rising chorus emissions in the magnetosphere, *J. Geophys. Res.*, *114*, A01203, doi:10.1029/2008JA013625.

Hikishima, M., Y. Omura, and D. Summers (2010), Microburst precipitation of energetic electrons associated with chorus wave generation, *Geophys. Res. Lett.*, *37*, L07103, doi:10.1029/2010GL042678.

Horne, R. B., and R. M. Thorne (1998), Potential waves for relativistic electron scattering and stochastic acceleration during magnetic storms, *Geophys. Res. Lett.*, *25*(15), 3011–3014.

Horne, R. B., et al. (2005), Wave acceleration of electrons in the Van Allen radiation belts, *Nature*, *437*, 227–230, doi:10.1038/nature03939.

Hospodarsky, G. B., T. F. Averkamp, W. S. Kurth, D. A. Gurnett, J. D. Menietti, O. Santolík, and M. K. Dougherty (2008), Observations of chorus at Saturn using the Cassini Radio and Plasma Wave Science instrument, *J. Geophys. Res.*, *113*, A12206, doi:10.1029/2008JA013237.

Inan, U. S., and R. A. Marshall (2011), *Numerical Electromagnetics: The FDTD Method*, Cambridge Univ. Press, Cambridge, U. K.

Katoh, Y., and Y. Omura (2007), Computer simulation of chorus wave generation in the Earth's inner magnetosphere, *Geophys. Res. Lett.*, *34*, L03102, doi:10.1029/2006GL028594.

Katoh, Y., and Y. Omura (2013), Effect of the background magnetic field inhomogeneity on generation processes of whistler-mode chorus and broadband hiss-like emissions, *J. Geophys. Res. Space Physics*, *118*, 4189–4198, doi:10.1002/jgra.50395.

Lee, J. H., and D. Kalluri (1999), Three-dimensional fdtd simulation of electromagnetic wave transformation in a dynamic inhomogeneous magnetized plasma, *IEEE Trans. Antennas Propag.*, *47*(7), 1146–1151.

Li, W., R. M. Thorne, J. Bortnik, Y. Y. Shprits, Y. Nishimura, V. Angelopoulos, C. Chaston, O. L. Contel, and J. W. Bonnell (2011a), Typical properties of rising and falling tone chorus waves, *Geophys. Res. Lett.*, *38*, L14103, doi:10.1029/2011GL047925.

Li, W., J. Bortnik, R. M. Thorne, Y. Nishimura, V. Angelopoulos, and L. Chen (2011b), Modulation of whistler mode chorus waves: 2. Role of density variations, *J. Geophys. Res.*, *116*, A06206, doi:10.1029/2010JA016313.

Li, W., R. M. Thorne, J. Bortnik, Y. Nishimura, and V. Angelopoulos (2011c), Modulation of whistler mode chorus waves: 1. Role of compressional Pc4-5 pulsations, *J. Geophys. Res.*, *116*, A06205, doi:10.1029/2010JA016312.

Nicholson, D. R. (1992), *Introduction to Plasma Theory*, Krieger Publishing Company, Malabar, Fla.

Nishimura, Y., et al. (2010), Identifying the driver of pulsating aurora, *Science*, *330*(6000), 81–84, doi:10.1126/science.1193130.

Nunn, D. (1990), The numerical simulation of VLF nonlinear wave-particle interactions in collision-free plasmas using the Vlasov hybrid simulation technique, *Comput. Phys. Commun.*, *60*, 1–25, doi:10.1016/0010-4655(90)90074-B.

Nunn, D., and Y. Omura (2012), A computational and theoretical analysis of falling frequency VLF emissions, *J. Geophys. Res.*, *117*, A08228, doi:10.1029/2012JA017557.

Nunn, D., Y. Omura, H. Matsumoto, I. Nagano, and S. Yagitani (1997), The numerical simulation of VLF chorus and discrete emissions observed on the Geotail satellite using a Vlasov code, *J. Geophys. Res.*, *102*(A12), 27,083–27,097.

Omura, Y., Y. Katoh, and D. Summers (2008), Theory and simulation of the generation of whistler-mode chorus, *J. Geophys. Res.*, *113*, A04223, doi:10.1029/2007JA012622.

Ossakow, S. L., E. Ott, and I. Haber (1972), Nonlinear evolution of whistler instabilities, *Phys. Fluids*, *15*(12), 2314–2326, doi:10.1063/1.1693875.

Reeves, G. D., et al. (2013), Electron acceleration in the heart of the Van Allen radiation belts, *Science*, *341*(6149), 991–994, doi:10.1126/science.1237743.

Santolík, O., D. A. Gurnett, J. S. Pickett, M. Parrot, and N. Cornilleau-Wehrlin (2003), Spatio-temporal structure of storm-time chorus, *J. Geophys. Res.*, *108*(A7), 1278, doi:10.1029/2002JA009791.

Santolík, O., D. A. Gurnett, J. S. Pickett, M. Parrot, and N. Cornilleau-Wehrlin (2004), A microscopic and nanoscopic view of storm-time chorus on 31 March 2001, *Geophys. Res. Lett.*, *31*, L02801, doi:10.1029/2003GL018757.

Tao, X., R. M. Thorne, W. Li, B. Ni, N. P. Meredith, and R. B. Horne (2011), Evolution of electron pitch-angle distributions following injection from the plasma sheet, *J. Geophys. Res.*, *116*, A04229, doi:10.1029/2010JA016245.

Tao, X., W. Li, J. Bortnik, R. M. Thorne, and V. Angelopoulos (2012), Comparison between theory and observation of the frequency sweep rates of equatorial rising tone chorus, *Geophys. Res. Lett.*, *39*, L08106, doi:10.1029/2012GL051413.

Thorne, R. M., B. Ni, X. Tao, R. B. Horne, and N. P. Meredith (2010), Scattering by chorus waves as the dominant cause of diffuse auroral precipitation, *Nature*, *467*, 943–946, doi:10.1038/nature09467.

Thorne, R. M., et al. (2013), Rapid local acceleration of relativistic radiation-belt electrons by magnetospheric chorus, *Nature*, *504*, 411–414, doi:10.1038/nature12889.

Trakhtengerts, V. Y. (1995), Magnetosphere cyclotron maser: Backward wave oscillator generation regime, *J. Geophys. Res.*, *100*(A9), 17,205–17,210.

Tsurutani, B. T., and E. J. Smith (1974), Postmidnight chorus: A substorm phenomenon, *J. Geophys. Res.*, *79*(1), 118–127.

Watt, C. E. J., A. W. Degeling, R. Rankin, K. R. Murphy, I. J. Rae, and H. J. Singer (2011), Ultralow-frequency modulation of whistler-mode wave growth, *J. Geophys. Res.*, *116*, A10209, doi:10.1029/2011JA016730.

Xiao, F., and X. Feng (2006), Modeling density and anisotropy of energetic electrons along magnetic field lines, *Plasma Sci. Technol.*, *8*(3), 279–284.

Xiao, F., R. M. Thorne, and D. Summers (1998), Instability of electromagnetic R-mode waves in a relativistic plasma, *Phys. Plasmas*, *5*(7), 2489–2497, doi:10.1063/1.872932.